High Confidence Visual Recognition of Persons by a Test of Statistical Independence

John G. Daugman

Abstract— A method for rapid visual recognition of personal identity is described, based on the failure of a statistical test of independence. The most unique phenotypic feature visible in a person's face is the detailed texture of each eye's iris: An estimate of its statistical complexity in a sample of the human population reveals variation corresponding to several hundred independent degrees-of-freedom. Morphogenetic randomness in the texture expressed phenotypically in the iris trabecular meshwork ensures that a test of statistical independence on two coded patterns originating from different eyes is passed almost certainly, whereas the same test is failed almost certainly when the compared codes originate from the same eye. The visible texture of a person's iris in a real-time video image is encoded into a compact sequence of multi-scale quadrature 2-D Gabor wavelet coefficients, whose most-significant bits comprise a 256-byte "iris code." Statistical decision theory generates identification decisions from Exclusive-OR comparisons of complete iris codes at the rate of 4000 per second, including calculation of decision confidence levels. The distributions observed empirically in such comparisons imply a theoretical "cross-over" error rate of one in 131 000 when a decision criterion is adopted that would equalize the false accept and false reject error rates. In the typical recognition case, given the mean observed degree of iris code agreement, the decision confidence levels correspond formally to a conditional false accept probability of one in about 10^{31}.

Index Terms— Image analysis, statistical pattern recognition, biometric identification, statistical decision theory, 2-D Gabor filters, wavelets, texture analysis, morphogenesis.

I. INTRODUCTION

EFFORTS to devise reliable mechanical means for biometric personal identification have a long and colorful history. In the Victorian era for example, inspired by the birth of criminology and a desire to identify prisoners and malefactors, Sir Francis Galton F.R.S. [13] proposed various biometric indices for facial profiles which he represented numerically. Seeking to improve on the system of French physician Alphonse Bertillon for classifying convicts into one of 81 categories, Galton devised a series of spring-loaded "mechanical selectors" for facial measurements and established an Anthropometric Laboratory at South Kensington [13]. Other biometric identifiers that have been adopted historically, ranging from cranial dimensions to digit length, as well as some of the numerous geometric facial measurements currently being tried, are described in [17], [25].

Today there is renewed interest in reliable, rapid, and unintrusive means for automatically recognizing the identity of persons. Security breaches in access to restricted areas at airports are known to have contributed to terrorism; and credit card fraud now costs six billion dollars annually [3]. Other applications for high confidence personal identification include passport control, bank automatic teller machines, protected access to premises or assets, law enforcement, government intelligence, entitlement verification, birth certificates, licenses, and any existing use of keys or cards. Some of the identifying biometric features now under investigation for potential use include hand geometry, blood vessel patterns in the retina or hand, fingerprints, voice-prints, and handwritten signature dynamics. The critical attributes for any such measure are: the number of degrees-of-freedom of variation in the chosen index across the human population, since this determines uniqueness; its immutability over time and its immunity to intervention; and the computational prospects for efficiently encoding and reliably recognizing the identifying pattern.

The possibility that the iris of the eye might be used as a kind of optical fingerprint for personal identification was suggested originally by ophthalmologists [1], [12], [24], who noted from clinical experience that every iris had a highly detailed and unique texture, which remained unchanged in clinical photographs spanning decades (contrary to the occult diagnostic claims of "iridology"). Among the visible features in an iris, some of which may be seen in the close-up image of Fig. 1, are the trabecular meshwork of connective tissue (pectinate ligament), collagenous stromal fibres, ciliary processes, contraction furrows, crypts, a serpentine vasculature, rings, corona, coloration, and freckles [1], [11], [12], [24]. The striated trabecular meshwork of chromatophore and fibroblast cells creates the predominant texture under visible light [24], but all of these sources of radial and angular variation taken together constitute a distinctive "fingerprint" that can be imaged at some distance from the person. Further properties of the iris that enhance its suitability for use in automatic identification include 1) its inherent isolation and protection from the external environment, being an internal organ of the eye, behind the cornea and the aqueous humor; 2) the impossibility of surgically modifying it without unacceptable risk to vision; and 3) its physiological response to light, which provides a natural test against artifice.

A property the iris shares with fingerprints is the random morphogenesis of its minutiae. Because there is no genetic
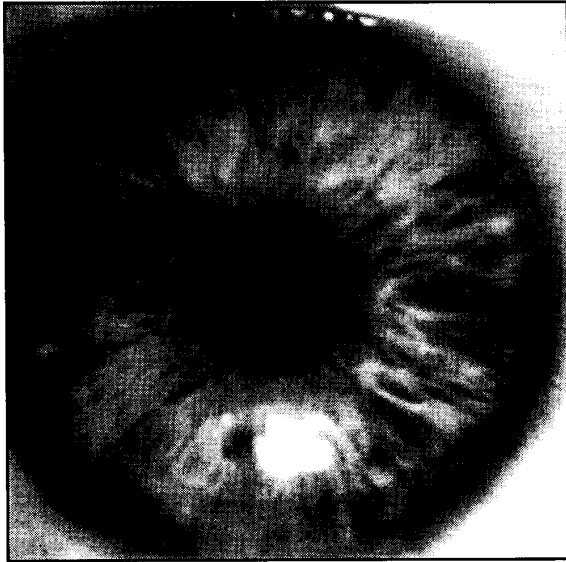
Fig. 1. Close-up image illustrating the trabecular meshwork and other features of a human iris.

penetrance in the expression of this organ beyond its anatomical form, physiology, color and general appearance, the iris texture itself is stochastic or possibly chaotic. Since its detailed morphogenesis depends on initial conditions in the embryonic mesoderm from which it develops [11], the phenotypic expression even of two irises with the same genetic genotype (as in identical twins, or the pair possessed by one individual) have uncorrelated minutiae. In these respects the uniqueness of every iris parallels the uniqueness of every fingerprint, common genotype or not. But the iris enjoys further practical advantages over fingerprints and other biometrics for purposes of automatic recognition, including 4) the ease of registering its image at some distance from the Subject without physical contact, unintrusively and perhaps inconspicuously; and 5) its intrinsic polar geometry, which imparts a natural coordinate system and an origin of coordinates.

Unknown until the present work was whether mathematically there were sufficient degrees-of-freedom, or forms of variation in the iris among individuals, to impart to it the same singularity as a conventional fingerprint. Also uncertain was whether efficient algorithms could be developed to extract a detailed iris description reliably from a live video image, generate a compact code for the iris (of minuscule length compared with image data size), and render a decision about individual identity with high statistical confidence, all within less than one second of computation time on a general-purpose microprocessor. The present report resolves all of these questions affirmatively and describes a working system.

II. IMAGE ANALYSIS

A. Operators for Locating an Iris

Iris analysis begins with reliable means for establishing whether an iris is visible in the video image, and then precisely locating its inner and outer boundaries (pupil and limbus). Because of the felicitous circular geometry of the iris, these tasks can be accomplished for a raw input image $I(x,y)$ by integrodifferential operators that search over the image domain (x,y) for the maximum in the blurred partial derivative, with respect to increasing radius r, of the normalized contour integral of $I(x,y)$ along a circular arc ds of radius r and center coordinates (x_0, y_0):

$$\max_{(r,x_0,y_0)} \left| G_\sigma(r) * \frac{\partial}{\partial r} \oint_{r,x_0,y_0} \frac{I(x,y)}{2\pi r} ds \right|, \qquad (1)$$

where $*$ denotes convolution and $G_\sigma(r)$ is a smoothing function such as a Gaussian of scale σ. The complete operator behaves in effect as a circular edge detector, blurred at a scale set by σ, that searches iteratively for a maximum contour integral derivative with increasing radius at successively finer scales of analysis through the three parameter space of center coordinates and radius (x_0, y_0, r) defining the path of contour integration.

At first the blurring factor σ is set for a coarse scale of analysis so that only the very pronounced circular transition from iris to (white) sclera is detected. Then after this strong circular boundary is more precisely estimated, a second search begins within the confined central interior of the located iris for the fainter pupillary boundary, using a finer convolution scale σ and a smaller search range defining the paths (x_0, y_0, r) of contour integration. In the initial search for the outer bounds of the iris, the angular arc of contour integration ds is restricted in range to two opposing 90° cones centered on the horizontal meridian, since eyelids generally obscure the upper and lower limbus of the iris. Then in the subsequent interior search for the pupillary boundary, the arc of contour integration ds in operator (1) is restricted to the upper 270° in order to avoid the corneal specular reflection that is usually superimposed in the lower 90° cone of the iris from the illuminator located below the video camera. Taking the absolute value in (1) is not required when the operator is used first to locate the outer boundary of the iris, since the sclera is always lighter than the iris and so the smoothed partial derivative with increasing radius near the limbus is always positive. However, the pupil is not always darker than the iris, as in persons with normal early cataract or significant back-scattered light from the lens and vitreous humor; applying the absolute value in (1) makes the operator a good circular edge-finder regardless of such polarity-reversing conditions. With σ automatically tailored to the stage of search for both the pupil and limbus, and by making it correspondingly finer in successive iterations, the operator defined in (1) has proven to be virtually infallible in locating the visible inner and outer annular boundaries of irises.

For rapid discrete implementation of the integrodifferential operator in (1), it is more efficient to interchange the order of convolution and differentiation and to concatenate them, before computing the discrete convolution of the resulting operator with the discrete series of undersampled sums of pixels along circular contours of increasing radius. Using the finite difference approximation to the derivative for a discrete

series in n,

$$\frac{\partial G_\sigma(r)}{\partial r} \approx G_\sigma^{(1)}(n) = \frac{1}{\Delta r} G_\sigma(n\Delta r) - \frac{1}{\Delta r} G_\sigma((n-1)\Delta r),$$

$$(2)$$

where Δr is a small increment in radius, and replacing the convolution and contour integrals with sums, we can derive through these manipulations an efficient discrete operator (see (3) at the bottom of the page) for finding the inner and outer boundaries of an iris where $\Delta\theta$ is the angular sampling interval along the circular arcs, over which the summed $I(x, y)$ pixel intensities represent the contour integrals expressed in (1).

A nonlinear enhancement of this operator makes it more robust for detecting the inner boundary of the iris. Because the circular edge that defines the pupillary boundary is often very faint, especially in dark-eyed persons, it is advantageous to divide each term in the convolution summation over k in (3) by a further contour integral around a smaller radius $(k-2)\Delta r$. This divisor becomes very small and stable as the parameters $(n\Delta r, x_0, y_0)$ of contour integration become well-matched to the true location and size of the pupil, and this helps the resulting sum of ratio terms (see (4) at the bottom of the page) to achieve a distinctive maximum that reliably locates the pupillary boundary. In essence, dividing by the second contour integral exploits the fact that the interior of the pupil is generally both homogeneous and dark. This creates a suddenly very small divisor when the parameters $(n\Delta r, x_0, y_0)$ are optimal for the true pupil, thus producing a sharp maximum in the overall search operator (4).

Using multigrid search with gradient ascent over the image domain (x, y) for the center coordinates and initial radius of each series of contour integrals, and decimating both the incremental radius interval Δr and the angular sampling interval $\Delta\theta$ in successively finer scales of search spanning four octaves, these iris locating operations become very efficient without loss of reliability. The total processing time on a RISC-based CPU for iris detection and localization to single-pixel precision using such operators, starting from a 640 x 480 image, is about one-quarter of a second (250 msec) with optimized integer code.

B. Assessing Image Quality, Eyelid Occlusion, and Possibility of Artifice

The operators previously described for finding an iris also provide a good assessment of "eyeness," and of the autofocus performance of the video camera. The normally sharp boundary at the limbus between the iris and the (white) sclera generates a large positive circular edge; if a derivative larger than a certain criterion is not detected by the searching operator using the contour integral defined in (3), then this suggests either that no eye is present, or that it is largely obscured by eyelids, or that it is in poor focus or beyond resolution. In practice the automatic identifying system that has been built continues to grab image frames in rapid succession until several frames in sequence confirm that an eye is present and in focus, through large values being found by operator (3), and through large ratios of circular contour integrals being found on either side of the putative limbus boundary. Excessive eyelid occlusion is alleviated in cooperating Subjects by providing live video feedback through the lens of the video camera into which the Subject's gaze is directed, by means of a miniature liquid-crystal TV monitor displaying the magnified image through a beamsplitter in the optical axis.

A further test for evidence that a living eye is present exploits the fact that pupillary diameter relative to iris diameter in a normal eye is constantly changing, even under steady illumination [1], [11]. Continuous involuntary oscillations in pupil size, termed hippus or pupillary unrest, arise from normal fluctuations in the activities of both the sympathetic and parasympathetic innervation of the iris sphincter muscle [1]. These changes in pupil diameter relative to iris diameter over a sequence of frames are detected by the discrete operators (4) and (3), respectively, in order to compute a "hippus measure" defined as the coefficient of variation (standard deviation divided by mean) for the fluctuating time series of these diameter ratios. Together with the accompanying elastic deformations in the iris texture itself arising either from normal hippus or from a light-driven pupillomotor response, these fluctuations could provide a test against artifice (such as a fake iris painted onto a contact lens) if necessary in highly secure implementations of this system.

$$\max_{(n\Delta r, x_0, y_0)} \left| \frac{1}{\Delta r} \sum_k \left\{ \left(G_\sigma((n-k)\Delta r) - G_\sigma((n-k-1)\Delta r) \right) \sum_m I\big[(k\Delta r \cos(m\Delta\theta)+x_0), (k\Delta r \sin(m\Delta\theta)+y_0)\big] \right\} \right|,$$

$$(3)$$

$$\max_{(n\Delta r, x_0, y_0)} \left| \sum_k \left\{ \frac{\left(G_\sigma((n-k)\Delta r) - G_\sigma((n-k-1)\Delta r) \right) \sum_m I\big[(k\Delta r \cos(m\Delta\theta)+x_0), (k\Delta r \sin(m\Delta\theta)+y_0)\big]}{\Delta r \sum_m I\big[((k-2)\Delta r \cos(m\Delta\theta)+x_0), ((k-2)\Delta r \sin(m\Delta\theta)+y_0)\big]} \right\} \right|.$$

$$(4)$$

C. Two-Dimensional Gabor Filters

An effective strategy for extracting both coherent and incoherent textural information from images, such as the detailed texture of an iris, is the computation of 2-D Gabor phasor coefficients. This family of 2-D filters were originally proposed in 1980 by Daugman [8] as a framework for understanding the orientation-selective and spatial-frequency-selective receptive field properties of neurons in the brain's visual cortex, and as useful operators for practical image analysis problems. Their mathematical properties were further elaborated by the author in 1985 [9], who pointed out that such 2-D quadrature phasor filters were conjointly optimal in providing the maximum possible resolution both for information about the orientation and spatial frequency content of local image structure ("what"), simultaneously with information about 2-D position ("where"). The complex-valued family of 2-D Gabor filters uniquely achieves the theoretical lower bound for conjoint uncertainty over these four variables, as dictated by an inescapable uncertainty principle [9].

These properties are particularly useful for texture analysis [2], [4]–[7], [10], [14]–[16], [18], [23], [29]–[31] because of the 2-D spectral specificity of texture as well as its variation with 2-D spatial position. A rapid method for obtaining the required coefficients on these elementary functions for the purpose of representing any image completely by its 2-D Gabor Transform, despite the non-orthogonality of the expansion basis, was given in [10] through the use of a relaxation network. A large and growing literature now exists on the efficient use of this nonorthogonal expansion basis and its applications (e.g., [2], [14], [23], [28]).

Two-dimensional Gabor filters over the image domain (x, y) have the functional form

$$G(x,y) = e^{-\pi\left[(x-x_0)^2/\alpha^2 + (y-y_0)^2/\beta^2\right]}$$
$$\cdot e^{-2\pi i[u_0(x-x_0)+v_0(y-y_0)]}, \qquad (5)$$

where (x_0, y_0) specify position in the image, (α, β) specify effective width and length, and (u_0, v_0) specify modulation, which has spatial frequency $\omega_0 = \sqrt{u_0^2 + v_0^2}$ and direction $\theta_0 = \arctan(v_0/u_0)$. (A further degree-of-freedom included below but not captured above in (5) is the relative orientation of the elliptic Gaussian envelope, which creates cross-terms in xy.) The 2-D Fourier transform $F(u, v)$ of a 2-D Gabor filter has exactly the same functional form, with parameters just interchanged or inverted [9]:

$$F(u,v) = e^{-\pi\left[(u-u_0)^2\alpha^2 + (v-v_0)^2\beta^2\right]} e^{-2\pi i[x_0(u-u_0)+y_0(v-v_0)]}.$$
$$(6)$$

The real part of one member of the 2-D Gabor filter family, centered at the origin $(x_0, y_0) = (0, 0)$ and with aspect ratio $\beta/\alpha = 1$ is shown in Fig. 2, together with its 2-D Fourier transform $F(u, v)$.

2-D Gabor functions can form a complete self-similar wavelet expansion basis [10], with the requirements of orthogonality and strictly compact support [20]–[21] relaxed, by appropriate parameterization for dilation, rotation, and translation. If we take $\Psi(x, y)$ to be a chosen generic 2-D Gabor wavelet, then we can generate from this member

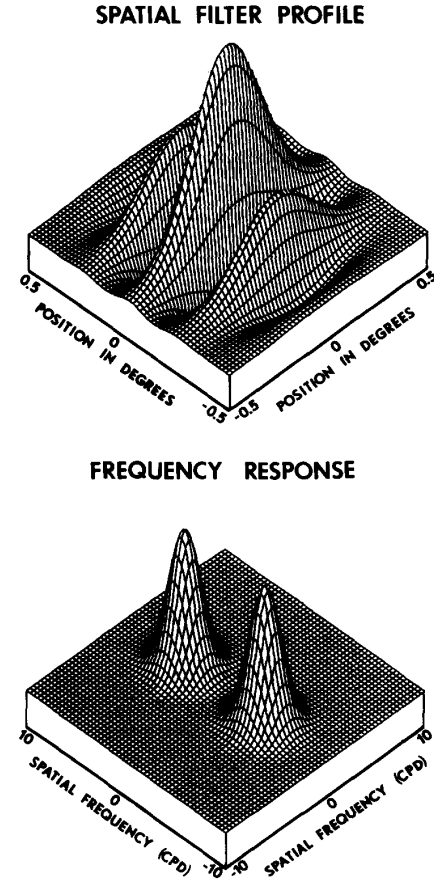**SPATIAL FILTER PROFILE**

FREQUENCY RESPONSE

Fig. 2. The real part of a 2-D Gabor wavelet, and its 2-D Fourier transform (from Daugman (1980) [8]).

a complete self-similar family of 2-D wavelets through the generating function

$$\Psi_{mpq\theta}(x,y) = 2^{-2m}\Psi(x',y'), \qquad (7)$$

where the substituted variables (x', y') incorporate dilations of the wavelet in size by 2^{-m}, translations in position (p, q), and rotations through angle θ:

$$x' = 2^{-m}[x\cos(\theta) + y\sin(\theta)] - p \qquad (8)$$

$$y' = 2^{-m}[-x\sin(\theta) + y\cos(\theta)] - q. \qquad (9)$$

It is noteworthy [9] that as consequences of the similarity theorem, shift theorem, and modulation theorem of Fourier analysis, together with the rotation isomorphism of the Fourier transform, all of these effects of the generating function (7) applied to a 2-D Gabor mother wavelet $\Psi(x, y) = G(x, y)$ in order to generate a 2-D Gabor daughter wavelet $\Psi_{mpq\theta}(x, y)$ have corresponding or reciprocal effects on its Fourier transform $F(u, v)$ without any change in functional form. This family of wavelet filters and their Fourier transforms is closed

under the transformation group of dilations, translations, rotations, and convolutions [9]. We will exploit these self-similarity properties of 2-D Gabor filters in analyzing iris textures across multiple scales to construct identifying codes.

D. Doubly Dimensionless Projected Polar Coordinate System

Zones of analysis are established on the iris in a doubly dimensionless projected polar coordinate system. Its purpose is to maintain reference to the same regions of iris tissue regardless both of pupillary constriction and overall iris image size, and hence regardless of distance to the eye and video zoom factor. This pseudo polar coordinate system is not necessarily concentric, since for most eyes the pupil is not central in the iris. (Typically the pupil is both nasal to, and inferior to, the center of the iris [1], and it is not unusual for its displacement to be as great as 15%.) The stretching of the elastic trabecular meshwork of the iris from constriction of the pupil is intrinsically modelled by the doubly dimensionless projected coordinate system as the stretching of a homogeneous rubber sheet, having the topology of an annulus anchored along its outer perimeter, with tension controlled by an off-centered interior ring of variable radius.

The homogeneous rubber sheet model assigns to each point in the iris, regardless of size and pupillary dilation, a pair of dimensionless real coordinates (r, θ) where r lies on the unit interval $[0,1]$ and θ is the usual angular quantity that is cyclic over $[0,2\pi]$. The remapping of the iris image $I(x, y)$ from raw coordinates (x, y) to the doubly dimensionless nonconcentric polar coordinate system (r, θ) can be represented as

$$I(x(r, \theta), y(r, \theta)) \rightarrow I(r, \theta) \tag{10}$$

where $x(r, \theta)$ and $y(r, \theta)$ are defined as linear combinations of both the set of pupillary boundary points $(x_p(\theta), y_p(\theta))$ around the circle that was found to maximize operator (4), and the set of limbus boundary points along the outer perimeter of the iris $(x_s(\theta), y_s(\theta))$ bordering the sclera, that was found to maximize operator (3):

$$x(r, \theta) = (1 - r)x_p(\theta) + rx_s(\theta) \tag{11}$$

$$y(r, \theta) = (1 - r)y_p(\theta) + ry_s(\theta). \tag{12}$$

Demarcations of the zones of analysis specified in this projected doubly dimensionless coordinate system, for two sample close-up iris images, are illustrated in Figs. 3 and 4. These zones of analysis are assigned in the same format for all eyes and are based on a fixed partitioning of the dimensionless polar coordinate system, but of course for any given eye their affine radial scaling depends on the actual pupillary diameter (and possible offset) relative to the limbus boundary as determined by operators (3) and (4). The zones of analysis always exclude a region at the top of the iris where partial occlusion by the upper eyelid is common, and a 45° notch at the bottom where there is a corneal specular reflection from the filtered light source that illuminates the eye from below.

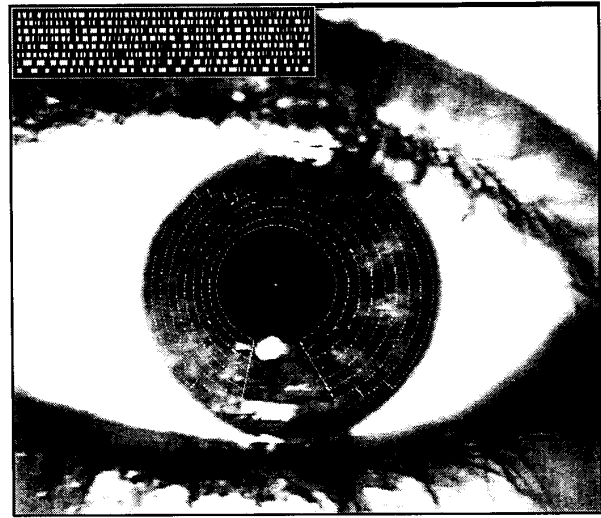Fig. 3. Demarcated zones of analysis and illustration of a computed iris code.

Fig. 4. Demarcated zones of analysis and illustration of a computed iris code.

(Illumination at an angle is desirable to deflect its specular reflection from eye-glasses, which persons are not asked to remove. The much greater curvature of the cornea compared with that of spectacle lenses, however, prevents elimination of the illuminator's first Purkinje reflection from the moist lower front surface of the cornea or of contact lenses; this necessitates the exclusion notch in the zones of analysis near the 6-o'clock position.)

Rotation invariance to correct for head tilt and cyclovergence of the eye within its orbit is achieved in a subsequent stage of analysis of the iris code itself. The overall recognition scheme is thus invariant under the Poincaré group of transformations of the iris image: planar translation, rotation (due to cyclovergence and tilt of the head), and dilation (due both to imaging distance and video zoom factor). Through the doubly dimensionless coordinate system, the constructed iris code is also invariant under the nonaffine elastic distortion (or projected conic transformation) that arises from variable pupil constriction.

III. Code Construction and Entropy Measures

An uncompressed code length of 256 bytes was chosen because this is roughly the capacity of the three-channel magnetic stripe affixed to the reverse side of the standard IS-7811 credit/debit card [3]. But this absolute code length only establishes an upper bound on the information capacity of an iris code, and it is important to know its actual inherent capacity. This capacity is reduced by intrinsic correlations, if any, among the coding primitives themselves. It is then also important to know the "source entropy" associated with the typical human iris signal, which will be much less than the upper bound determined by the resolution of imaging, because of inherent correlations (especially radial) within the iris. These reduced entropies directly influence the confidence levels associated with any decision strategy. In the methods to be described here, irises are efficiently recognized by executing a statistical test of independence on their codes. In effect, this examines whether the degree to which one iris code predicts another iris code, is compatible with the hypothesis that they arise from independent random processes. Such a test of statistical independence is passed almost certainly for two iris codes from different eyes, but the same test is failed almost certainly when the compared signatures originate from the same eye.

A. The 256-Byte Iris Code

The 2-D Gabor filters used for iris recognition are defined in the doubly dimensionless polar coordinate system (r, θ) as follows:

$$G(r, \theta) = e^{-i\omega(\theta-\theta_0)} e^{-(r-r_0)^2/\alpha^2} e^{-(\theta-\theta_0)^2/\beta^2}. \quad (13)$$

Both the real and imaginary members of such quadrature filters are employed, so the resulting image projections are complex. The real parts of the 2-D Gabor filters are slightly adjusted through truncation to give them zero volume, and hence no dc response, so that computed iris code bits do not depend upon strength of illumination. (The imaginary parts of the filters inherently have no dc response because of odd symmetry.) The parameters α and β co-vary in inverse proportion to ω to generate a self-similar, multi-scale wavelet family of 2-D frequency-selective quadrature filters with constant logarithmic bandwidth, whose locations, specified by θ_0 and r_0, range across the zones of analysis of the iris.

Each bit h in an iris code can be regarded as a coordinate of one of the four vertices of a logical unit square in the complex plane. It is computed by evaluating, at one scale of analysis, the sign of both the real and imaginary parts of the quadrature image projections from a local region of the iris image $I(\rho, \phi)$ onto a particular complex 2-D Gabor filter:

$$h_{\text{Re}} = 1 \text{ if } \text{Re} \int_\rho \int_\phi e^{-i\omega(\theta_0-\phi)} e^{-(r_0-\rho)^2/\alpha^2}$$
$$\cdot e^{-(\theta_0-\phi)^2/\beta^2} I(\rho, \phi)\rho d\rho d\phi \geq 0, \quad (14)$$

$$h_{\text{Re}} = 0 \text{ if } \text{Re} \int_\rho \int_\phi e^{-i\omega(\theta_0-\phi)} e^{-(r_0-\rho)^2/\alpha^2}$$

$$\cdot e^{-(\theta_0-\phi)^2/\beta^2} I(\rho, \phi)\rho d\rho d\phi < 0, \quad (15)$$

$$h_{\text{Im}} = 1 \text{ if } \text{Im} \int_\rho \int_\phi e^{-i\omega(\theta_0-\phi)} e^{-(r_0-\rho)^2/\alpha^2}$$
$$\cdot e^{-(\theta_0-\phi)^2/\beta^2} I(\rho, \phi)\rho d\rho d\phi \geq 0, \quad (16)$$

$$h_{\text{Im}} = 0 \text{ if } \text{Im} \int_\rho \int_\phi e^{-i\omega(\theta_0-\phi)} e^{-(r_0-\rho)^2/\alpha^2}$$
$$\cdot e^{-(\theta_0-\phi)^2/\beta^2} I(\rho, \phi)\rho d\rho d\phi < 0. \quad (17)$$

Thus, a single complex 2-D Gabor filter (13), having a particular set of size and position parameters $(r_0, \theta_0; \alpha, \beta, \omega)$ in the dimensionless iris domain (r, θ), performs a coarse phase quantization of the local texture signal by approximating it as one vertex $(h_{\text{Re}}, h_{\text{Im}})$ of the logical unit square associated with this filter through conditionals (14)–(17). The time required for computing a complete iris code of 2 048 such paired bits (256 bytes) on a RISC-based CPU, once an iris has been located within the image, is about one-tenth of a second (100 msec) with optimized integer code.

B. Commensurability of Iris Codes

A critical feature of this coding approach is the achievement of commensurability among iris codes, by mapping all irises into a representation having universal format and constant length, regardless of the apparent amount of iris detail. In the absence of commensurability among the codes, one would be faced with the inevitable problem of comparing long codes with short codes, showing partial agreement and partial disagreement in their lists of features. It is not obvious mathematically how one would make objective decisions and compute confidence levels on a rigorous basis in such a situation. This difficulty has hampered efforts to automate reliably the recognition of fingerprints. Commensurability facilitates and objectifies the code comparison process, as well as the computation of confidence levels for each decision. It thereby greatly increases both the speed and the reliability of iris recognition decisions.

C. Bitwise Entropy and Iris Variation

A primary question is whether there is independent variation in iris detail, both within a given iris and across the human population. Any systematic correlations in iris detail across the population would undermine the uniqueness of an iris code. Similarly, any systematic correlations within an iris would reduce its statistical complexity, or dimensionality, and thus also undermine its uniqueness.

A code of any length has maximum information capacity if all its possible states are equiprobable [26]. This reflects the fact that the Shannon entropy measure

$$S = -\sum_{j=1}^n P_j \log_2 P_j, \quad (18)$$

for P_j the probability of each of the n states and with

$$\sum_{j=1}^{n} P_j = 1 \qquad (19)$$

is maximum when for all j,

$$P_j = 1/n. \qquad (20)$$

By construction, the 2-D Gabor filters (13) have no DC response in either their real or imaginary parts, as noted earlier. This eliminates possible dependency of the computed code bit conditionals (14)–(17) on mean illumination of the iris and on its contrast gain, and it also renders equiprobable the four vertices of the logical unit square $(h_{\text{Re}}, h_{\text{Im}})$ associated with each 2-D Gabor filter. As a consequence of analyzing the iris texture with filters lacking any dc response, the iris code has the property of encoding zero-crossings, which are known [19] to be exceedingly rich in information for band-limited signals.

The variation among iris code bits as defined above in (14)–(17) was tracked both across bit location within the code and across a population of 592 different iris codes. The ethnic groups and nationalities included in this sample are listed in Section V-A, together with further database details. For each of 128 code bit locations, drawn from all parts of the iris code, Fig. 5 plots the probability of a set bit. The graph shows that this is fairly equiprobable across all code bit locations, and that it remains close to one-half. (Mean of the means is 0.4984 ± 0.0244). The flatness of the graph reflects the existence of independent variation in the detailed iris texture, both across an iris and across the human population studied. The amount of independent variation that is typical in a given iris will be quantified in the following section, which estimates the underlying number of independent degrees-of-freedom in an iris code after its intrinsic correlations have been factored out. Across the population, the constant independent probability of any given code bit being set (i.e., the full equivocation entropy between iris codes) presumably reflects the absence of genetic penetrance in the detailed morphogenesis of this tissue, in favor of stochastic or chaotic processes. Any systematic feature, say at the 12-o'clock position in the iris, would have caused systematic deviation in Fig. 5 for the bit probabilities derived from that region. Second, this graph's proximity to a probability of one-half establishes that, since very nearly $p = 1 - p$, the iris code is bitwise a maximum entropy code.

D. Number of Independent Degrees-of-Freedom in an Iris Code

Although there are 256 bytes or 2 048 bits in any given iris code, such a code possesses far fewer than 2 048 independent binary degrees-of-freedom. One reason is that there are substantial radial correlations within an iris. For example, a given furrow or ciliary process tends to propagate across a significant radial distance in the iris, exerting its influence on several remote parts of the code, thus reducing their independence. Similarly, a feature such as a furrow influences different parts of the code associated with several different scales of analysis, since the Fourier spectrum of such a punctate feature can span several octaves. Finally, inherent correlations are introduced by the bandpass property of the 2-D Gabor filters, specifically
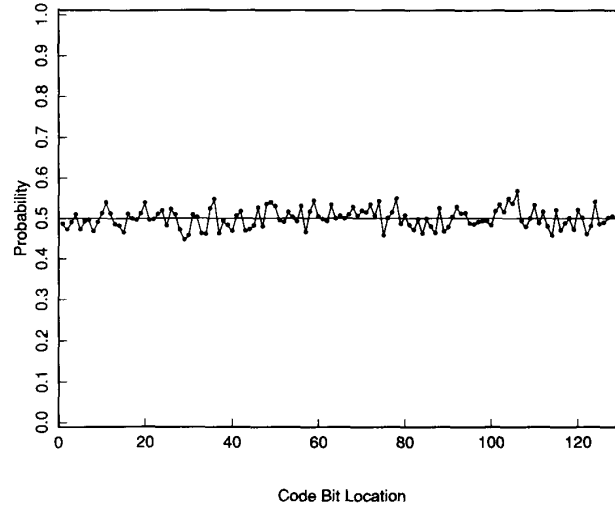
Bit Probabilities

Fig. 5.   Equiprobable variation of iris code bits, for each of 128-code bit locations, across a population of 592 different iris codes.

by the finite bandwidth determined by parameters α, β, and ω in (13).

As pointed out by Wiener [32], any signal convolved with a linear filter acquires a correlation distance that is greater than or equal to the reciprocal of the bandwidth of the filter. This property is well-known for low-pass filters but is perhaps less widely recognized for bandpass filters. Even though the peak response of the bandpass filter might be at a very high frequency, its passband introduces phase coherence that lingers for a greater number of cycles, the narrower its bandwidth. (This is easily grasped by considering the limiting case of the coherent response generated by a notch-pass filter.) In the present case, the correlations introduced inherently by the band-limited 2-D Gabor filters alone reduce the information capacity of the iris code by a factor of 4.05, from 2 048 bits to about 506 bits, given the values of α, β, ω and the sampling densities employed at the different scales of analysis.

The number of independent degrees-of-freedom typically remaining in an iris code after both of these sources of correlation have been factored in (those arising from the 2-D Gabor filters and those inherent within an iris), can be estimated by examining the distribution of Hamming distances computed across a population of unrelated iris codes. Comparing each pair of iris codes A and B bit-by-bit, their normalized Hamming distance HD is defined here as the fraction of disagreeing bits between them:

$$HD = \frac{1}{2,048} \sum_{j=1}^{2,048} A_j(\text{XOR})B_j \qquad (21)$$

where the Boolean operator (XOR) equals 1, if and only if the two bits A_j and B_j are different.

Since each bit of any iris code has equal *a priori* odds of being a 1 or a 0, there is probability $p = 0.5$ that any pair
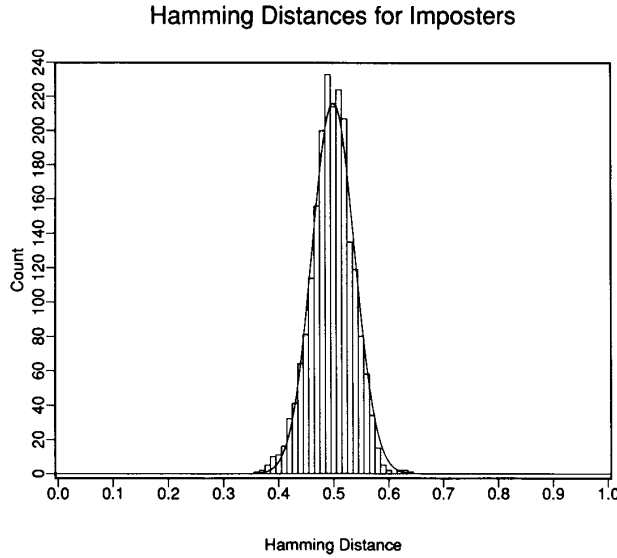
Hamming Distances for Imposters

Fig. 6. Distribution of Hamming distances between unrelated iris codes. Solid curve is (22).

of bits from different iris codes disagree. (Each of the four states 00, 01, 10, 11 has probability 0.25; the bits agree in two cases and disagree in the other two.) If each of the 2,048 bits in a given iris code were fully independent of every other bit, then the expected distribution of observed Hamming distances between two independent such iris codes would be a binomial distribution with $p = 0.5$ and $N = 2048$ (in other words, equivalent to tossing a fair coin 2048 times, and counting the fraction of heads in each round of 2048 tosses). Once the intrinsic code correlations introduced by the 2-D Gabor filters were factored in, the distribution should be a binomial with $p = 0.5$ and $N = 506$ if the iris itself had no inherent correlations.

The actual distribution of observed Hamming distances between codes for different irises is shown in Fig. 6, which is generated from 2064 complete comparisons between unrelated pairs of iris codes. This empirical distribution has a standard deviation of $\sigma = 0.038$, with a mean of $\mu = 0.497$. Since the standard deviation of a binomial distribution is given by $\sigma = \sqrt{pq/N}$ (where $q = 1 - p$), this distribution of Hamming distances would correspond to a binomial process with $N = 173$ Bernoulli trials per run. Given the estimate of roughly a four-sample correlation distance introduced by the 2-D Gabor encoders, we can now estimate that a bound on the "source entropy," reflecting the number of degrees-of-freedom of variation typical of iris texture resolved to 2048 samples, would be something like 690 bits.

The binomial distribution for N Bernoulli trials with outcome probabilities p and q predicts that the likelihood of observing a fraction $x = m/N$ events among the N trials is:

$$f(x) = \frac{N!}{m!(N - m)!} p^m q^{(N-m)}. \tag{22}$$

A theoretical plot of the probability density function associated with such a binomial process having $N = 173$ and $p = 0.5$ is also shown in Fig. 6 as a smooth curve, and it offers a good fit to the data. In summary it appears that there exist the equivalent of about 173 independent binary degrees-of-freedom typically remaining in a 2048-bit iris code, once both the correlations introduced by the 2-D Gabor filters and those inherent in the iris have been factored in. The likelihood of two iris codes from different irises agreeing completely by chance is thus roughly one in 2^{173}, or approximately 10^{-52}.

IV. STATISTICAL DECISION THEORY

The problem of recognizing the signature of a given iris as belonging to a particular individual, either after exhaustive search through a large database or just by comparison with a single authentication template, can be formulated within the framework of statistical decision theory [22], [27]. This framework also resolves the critical problem of assigning a confidence level to any such recognition decision. By this approach we can convert the problem of pattern recognition into a much more expedient task, which is the execution of a simple test of statistical independence.

A. Neyman–Pearson Formalism

Yes/No recognition decisions have four possible outcomes: either a given pattern is, or is not, a true instance of the category in question; and in either case, the decision made by the algorithm may be either the correct one or the incorrect one. In the present application the four possible outcomes are termed Acceptance of Authentic (AA), Acceptance of Imposter (IA), Rejection of Authentic (AR), and Rejection of Imposter (IR). Obviously the first and fourth outcomes are desired, and the second and third outcomes are errors. The goal of the decision-making algorithm is to maximize the conditional probabilities of AA and IR, while minimizing the likelihoods of IA and AR. The pairwise trade-offs among the probabilities of these four outcomes can be manipulated in a way that reflects their associated costs and benefits in a particular application.

The Neyman–Pearson formalism for decision problems in which the prior probabilities are not known and the error costs are not fixed, but the posterior distributions are known, is summarized in Fig. 7. A given measurement of the Hamming distance between two iris codes constitutes a point on the abscissa. This measurement is regarded as being a sample from one of two random processes ("Authentics" or "Imposters"), whose probability distributions have been arbitrarily shown here as Gaussians with large overlap for purposes of illustration. The two distributions, $P_{Au}(x)$ and $P_{Im}(x)$, specify respectively the probability density of a particular measured Hamming distance, x, arising from two comparisons of the same iris, or from two comparisons of different irises. Any measured Hamming distance smaller than a chosen decision criterion, as indicated by the dotted line in Fig. 7, is judged to belong to the Authentics distribution, while any Hamming distance greater than this criterion is judged to belong to the Imposters distribution. The probabilities of the four possible
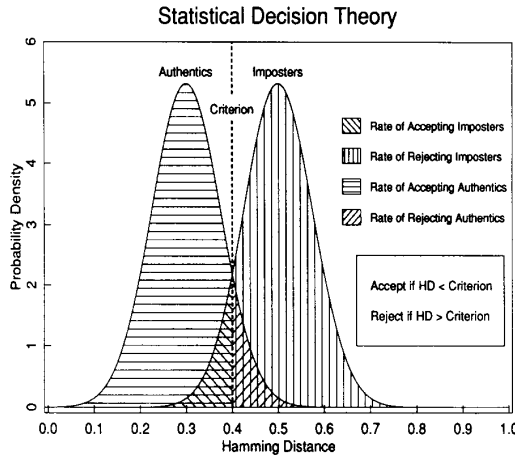
Statistical Decision Theory

Fig. 7. Statistical decision theory: Formalism for decisions under uncertainty.

Decision Strategies

Fig. 8. The Neyman–Pearson decision strategy curve.

outcomes AA, IA, AR, and IR are equal to the areas under the two probability density functions, $P_{\mathrm{Au}}(x)$ and $P_{\mathrm{Im}}(x)$, on either side of the chosen decision criterion C:

$$P(AA) = \int_0^C P_{\mathrm{Au}}(x)dx, \tag{23}$$

$$P(AR) = \int_C^1 P_{\mathrm{Au}}(x)dx, \tag{24}$$

$$P(IA) = \int_0^C P_{\mathrm{Im}}(x)dx, \tag{25}$$

$$P(IR) = \int_C^1 P_{\mathrm{Im}}(x)dx. \tag{26}$$

These four probabilities are represented by the four shaded areas in Fig. 7.

B. Strategies and Decidability

It is clear that the four probabilities separate into two pairs that must sum to unity, and two pairs are governed by inequalities:

$$P(\mathrm{AA}) + P(\mathrm{AR}) = 1, \tag{27}$$

$$P(\mathrm{IA}) + P(\mathrm{IR}) = 1, \tag{28}$$

$$P(\mathrm{AA}) > P(\mathrm{IA}), \tag{29}$$

$$P(\mathrm{IR}) > P(\mathrm{AR}). \tag{30}$$

It is also clear that the error rates, $P(\mathrm{AR})$ and $P(\mathrm{IA})$, could be minimized if the two Hamming distance distributions, $P_{\mathrm{Au}}(x)$ and $P_{\mathrm{Im}}(x)$, had minimal overlap. Their overlap
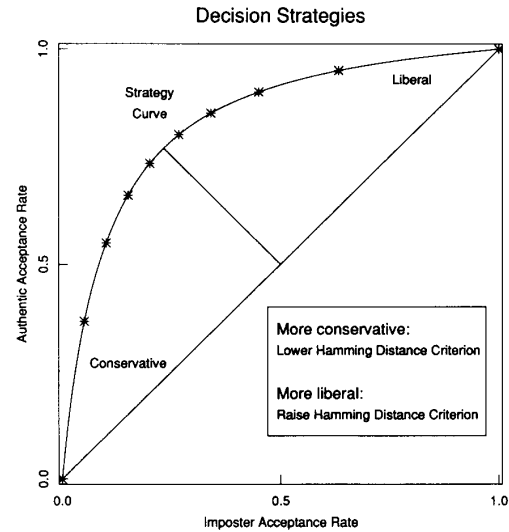
would be reduced if their two means were farther apart, or if their variances were smaller, of both. Of course, the two distributions in general will not be matched in form and variance, as was implied in Figure 7 for simplicity.

Manipulation of the decision criterion C in (23)–(26), in order to implement different decision strategies appropriate for the costs of either type of error in a given application, is illustrated schematically in Fig. 8. Such a decision strategy diagram, sometimes called a receiver operating characteristic or Neyman–Pearson curve, plots $P(\mathrm{AA})$ from (23) against $P(\mathrm{IA})$ from (25) as a locus of points. Each point in such a plot represents a decision strategy as specified by a different choice for the criterion C, as was indicated schematically in Fig. 7.

Inequality (29) states that the Neyman–Pearson strategy curve shown in Fig. 8 will always lie above the diagonal line. Clearly, strategies that were excessively conservative or excessively liberal would correspond to sliding along the curve towards the two diagonal extremes. Independent of where the decision criterion is placed along this continuum, the overall power of a pattern recognition method may be gauged by the length of the line segment in Fig. 8 joining the diagonal line and the bend in the strategy curve. This distance is monotonically related to the quantity d', for "detectability" or "decidability," defined as the difference between the means of the two distributions that were shown schematically in Fig. 7 divided by a conjoint measure of their standard deviations. This standard measure of statistical decidability has a value of about $d' = 8.4$ in the present work.

V. PERFORMANCE

With this biometric recognition problem now formulated within the frameworks of signal processing and statistical decision theory, we can evaluate the identifiability of persons by their irises.

A. Database

The performance results reported here are based partly on a photographic database of eye images generously made available in 1989 by Ophthalmology Associates of Connecticut, which were digitized and then combined with further databases of images subsequently acquired directly with video cameras in Massachusetts and in Cambridgeshire, England. The total number of different eyes represented in the combined database was 592, in images acquired over a three year period from 323 persons. Multiple images were always acquired from each person, ranging from 2 to 10 images of each eye over the time period (average 3.04 images per eye). Some images were rejected manually because of excessive eyelid closure or poor focus, before the automatic operators to perform these tasks as described in Section 2.2 were developed. Images in RS-170, VHS (NTSC), and S-VHS (NTSC) formats were digitized by 480 x 640 monochrome 8-bit/pixel framegrabber boards in either Macintosh or (by SCSI interface) SUN sparcstation hosts. Image resolution and iris size within the images varied due to both distance and video zoom factor, but the outer diameter of the iris was always greater than 60 pixels and was usually in the range of 100 pixels to 200 pixels. Imaging distances ranged from 46 cm to 15 cm, normally through a 330-mm positive meniscus lens. Ethnic groups and nationalities represented in the combined databases included persons of Northern European, Mediterranean, Eastern European, Indian, Semitic, Afro-American, Hispanic-American, Japanese, and Chinese origin.

B. Imposters' Hamming Distances

The distribution of Hamming distances generated by 2 064 direct comparisons between pairwise unrelated iris codes was seen previously in Fig. 6. The average Hamming distance was very close to 0.5 since any pair of corresponding bits in the codes for two different irises have equal probability of agreeing or disagreeing. The raw distribution was well described by a suitably fitted binomial model, whose effective number of implicit Bernoulli trials was appropriately reduced to factor out the residual correlations that exist among the bits within a given iris code.

Because of possible cyclovergence of the eye in its orbit as well as tilting of the head, all iris code comparisons must be performed over a range of relative orientations. The comparison process then becomes a "best of n" test of agreement, and this must be factored into the statistical decision theory that underlies this method of personal identification. Let $f_0(x)$ be the raw density distribution obtained for the Hamming distances between imposters after testing only at a single relative orientation; for example, $f_0(x)$ might be the binomial defined in (22). Then $F_0(x)$, the cumulative of $f_0(x)$ from 0 to x, becomes the probability of making a False Accept in such a test when using Hamming distance criterion x:

$$F_0(x) = \int_0^x f_0(x)dx \qquad (31)$$
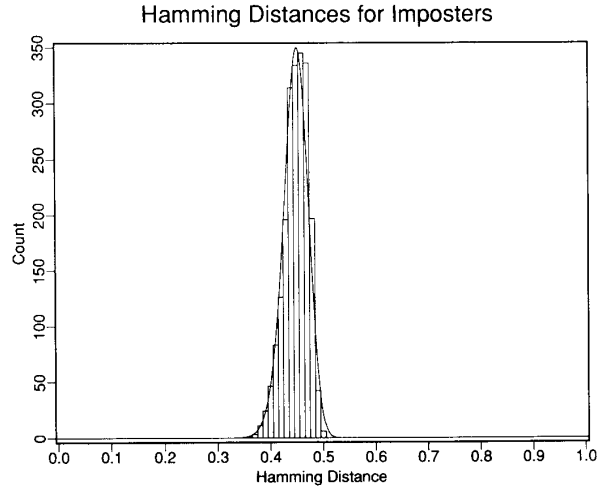
Hamming Distances for Imposters

Fig. 9. Hamming distances between unrelated iris codes, allowing for $n = 7$ different degrees of eye or head tilt. Solid curve is (34).

or, equivalently,

$$f_0(x) = \frac{d}{dx}F_0(x). \qquad (32)$$

Clearly, then, the probability of *not* making a false accept when using criterion x is $1 - F_0(x)$ after a single test, and it is $[1 - F_0(x)]^n$ after carrying out n such tests independently at n different relative orientations. It follows that the probability of a False Accept after a "best of n" test of agreement, when using criterion x, is

$$F_n(x) = 1 - [1 - F_0(x)]^n \qquad (33)$$

and the expected density $f_n(x)$ associated with this cumulative is

$$f_n(x) = \frac{d}{dx}F_n(x)$$
$$= nf_0(x)[1 - F_0(x)]^{n-1}. \qquad (34)$$

Fig. 9 shows the distribution of Hamming distances obtained from 2 064 pairwise comparisons among the same set of unrelated iris codes as was used in Fig. 6, but allowing for $n = 7$ different relative orientations of the eye. The distribution is biased toward a lower mean Hamming distance of $\mu = 0.450$, since only the best level of agreement after all seven rotations (i.e., the smallest Hamming distance) is kept and registered as the degree of match. The solid curve in Fig. 9 is a plot of (34), using as its $f_0(x)$ term the binomial density distribution specified earlier in (22) and plotted in Figure 6, and using the cumulative of this as its $F_0(x)$ term.

C. Authentics' Hamming Distances

Fig. 10 shows the distribution of Hamming distances computed between 1,208 pairs of different images of given irises ("authentics"). Different images of the same iris never yield a Hamming distance of zero, because of variations in the Subject's angle of gaze, degree of eyelid occlusion, specular
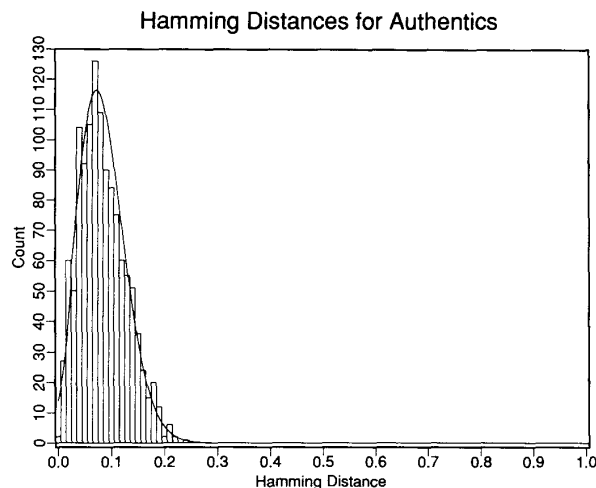
Fig. 10. Hamming distances between pairs of different iris codes for each given iris, allowing for $n = 7$ different degrees of eye or head tilt.
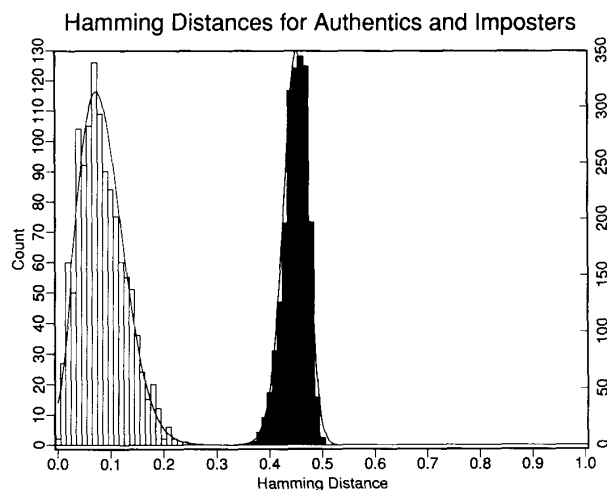

Fig. 11. Hamming distances for authentics and imposters, combined from Figs. 9 and 10.

reflections from the cornea or corrective lenses, random silhouettes of the eyelashes upon the iris, and light-driven as well as uncontrolled oscillations in pupillary dilation ("hippus") which cause some folding and unfolding of iris tissue that would not be captured by the homogeneous rubber sheet model. Nonetheless, these Hamming distances (again with 7 possible relative orientations of the eye) are clearly substantially smaller than those seen in Fig. 9 for imposters. This distribution has a mean of $\mu = 0.084$ and standard deviation $\sigma = 0.0435$. The solid curve plots a binomial as defined previously in (22) but with $p = 0.084$, and $N = 41$ chosen in order to match the observed σ since the standard deviation of a binomial distribution is $\sigma = \sqrt{pq/N}$ where $q = 1 - p$. Continuous interpolation of these binomial distributions, as well as estimation of their factorial terms, was done by Stirling's approximation which errs by less than 1% for $n \geq 9$:

$$n! \approx e^{n \ln(n) - n + \frac{1}{2} \ln(2\pi n)}. \tag{35}$$

D. Equivalent Bernoulli Trials

The distributions of Hamming distances for 2,064 pairwise comparisons of "imposters" (summed across pairwise unrelated iris codes), and for 1 208 pairwise comparisons of "authentics" accumulated separately, are shown together for comparison in Fig. 11. They are clearly well separated, with no empirical overlap and with no observations whatever falling in the region of 0.25 to 0.35 Hamming distance. These superimposed density distributions should be compared with Fig. 7, which represented the classic two-choice decision problem from statistical decision theory.

Each bit in an iris code is a random variable, and thus comparisons between iris codes are comparisons between ensembles of random variables. We have seen that on average, when comparing two iris codes obtained at different times from the same ("authentic") iris and making provision for possible head/eye tilt, any pair of corresponding bits have a probability of 0.084 of not matching. Similarly, we have seen that with

the same provision any pair of corresponding bits in two iris codes computed from different irises ("imposters"), have a probability of 0.450 of not matching.

Asking whether a given pair of iris codes were generated by the same iris, or by different irises, is then formally equivalent to the task of discovering to which of two possible classes a given coin belongs. For one type of coin the probability of heads is $p = 0.084$, and for the other type it is $p = 0.450$; and the method for finding out which one it is, is to toss the coin many times. Needless to say, sufficiently many tosses could resolve the question about which type of coin it was with enormously high confidence. The shapes of the two distributions shown in Figure 11 would have been expected using about 480 tosses of the $p = 0.450$ coin, and using about 40 tosses of the $p = 0.084$ coin, respectively, in each run of trials.

E. Decision Confidence Levels

The Bernoulli representation noted above for this pattern recognition task clarifies the calculation of confidence levels associated with any decision, including extrapolation of confidence levels into the region between the two distributions where no Hamming distances were observed empirically. As specified in (23)–(26), the conditional probabilities of personal identity or nonidentity given a particular observation can be calculated as the cumulative integrals under the two density distributions, taken from opposite directions up to whatever Hamming distance was observed. More generally, for any given operating choice of Hamming distance criterion, the latent probabilities of the two types of errors can be calculated by evaluating these cumulative integrals up to the chosen operating criterion.

Empirically, comparisons of iris codes computed from the available database of eye images produced no Hamming distances in the range of 0.25 to 0.35, so the use of any criterion in this range would produce 100% correct performance. However, the natures of the two distributions seen in

TABLE I
PERFORMANCE TABULATED AS ERROR PROBABILITIES
FOR SEVERAL DECISION CRITERIA

	Performance	
HD Criterion	Odds of False Accept	Odds of False Reject
0.25	1 in 13.5 billion	1 in 1 490
0.26	1 in 2.04 billion	1 in 2 660
0.27	1 in 339 million	1 in 4 850
0.28	1 in 60 million	1 in 9 000
0.29	1 in 12 million	1 in 17 100
0.30	1 in 2.4 million	1 in 32 800
0.31	1 in 603 000	1 in 64 200
0.32	1 in 151 000	1 in 128 000
0.33	1 in 39 800	1 in 260 000
0.34	1 in 11 500	1 in 536 000
0.35	1 in 3 630	1 in 1.12 million

Figure 11 and described by (22) and (34), allow us to calculate theoretical probabilities for False Accept and False Reject over this range. These probabilities are tabulated in Table 1. As the operating criterion is increased, the theoretical probability of a False Accept of course increases, while that of a False Reject decreases. The cross-over error rate occurs at a Hamming distance criterion of about 0.321, at which point both the False Accept error rate and the False Reject error rate are, theoretically, one in 131 000. This cross-over error rate suggests adopting a Hamming distance close to 0.32 as a balanced operating criterion, although of course more conservative or more liberal decision criteria may be more suitable for different applications. Any such criterion is easily implemented, with performance consequences as listed in Table I.

Finally, it is interesting to examine the posterior confidence levels associated with "typical" decisions for accepting an authentic, and for rejecting an imposter. The means of the two distributions in Fig. 11 indicate typicality. In the typical imposter comparison, which generates a Hamming distance of 0.45 after the "best of n" provision for eye rotation or head tilt, the confidence with which the subject is rejected (given this observation) corresponds to a conditional false reject probability one in $10^{9.6}$, or one in 4 billion. In the typical authentic comparison, which generates a Hamming distance of only 0.084, the confidence with which the Subject is accepted (given this observation) corresponds to a conditional false accept probability of one in 10^{31}.

F. Ergonomics, Robustness to Noise, and Imaging Factors

In many respects, the iris of the eye is inherently difficult to image at a comfortable "social" distance (e.g., several feet from a mounted video camera). It is a small tissue only 11 mm in diameter, and hence optical zoom is required, which creates problems of target motion amplification and limited depth of field for focus. More critical even than these limitations of spatial resolution is the limitation of grey-scale resolution, since without appropriate gain control of the video signal, many very darkly pigmented irises tend to be digitized flatly into only the lowest few states of an 8-bit A-to-D converter and thus reveal little structure. A further

reason that spatial resolution is less of a challenge than grey-scale resolution is because the upper roll-off frequency of the multi-scale bandpass 2-D Gabor encoders can be equated to a "blur circle" always larger than three pixels in diameter, which effectively makes any spatial resolution sharper than this irrelevant. Significant parts of the multiscale iris code are based on analysis of the coarser modulations of this mottled tissue; indeed, some of the 2-D Gabor encoders that are deployed subtend as much as a 70° angle around the pupil. In addition to these issues of resolution, a further challenge arises from the fact that unpredictable amounts of the iris may be occluded by eyelids or corrupted by random silhouettes of the eyelashes.

All of these factors contribute to the observation that different images of the same eye at different times may generate iris codes that disagree in as many as 25% of their bits (the highest observed Hamming distance in Fig. 10, for "authentics"). This percentage would be the net result, for example, if only half of the bits were deterministic and matched perfectly, while the entire other half were completely random and hence agreed just by chance half the time, yielding an overall agreement of 75% and thus a 0.25 normalized Hamming distance. The robustness of the present recognition method under such high levels of pattern degradation, noise, and inherent imaging limitations, is only possible because of the high statistical complexity associated with the myriad degrees-of-freedom in the iris signal. It is the consequent narrowness of the distribution of Hamming distances for unrelated eyes (the "Imposters" black distribution shown in Figure 11) that makes any Hamming distance significantly lower than 0.35 virtually impossible to achieve from independent random processes, i.e., unrelated eye images. Thus, the hypothesis of independence can be strongly rejected over all but a narrow range of possible Hamming distances.

It is perhaps illuminating that at the "cross-over" Hamming distance of 0.321, at which point confidence against both types of errors is better than 1 in 10^5, the level of image degradation or mismatch that is tolerated would be equivalent to obscuring fully two-thirds of the iris (producing just chance 50% agreement among those bits) while finding complete agreement among the remaining one-third of the bits. This extreme example illustrates the robustness against occlusion and noise that can be achieved by converting a pattern recognition problem into a test of statistical independence with a sufficiently large number of degrees-of-freedom.

G. Speed of Decision Making

The Bernoulli trial XOR formulation of the decision problem allows us to exploit the 32-bit architecture of a CPU for 16-fold parallelization. Since iris code comparisons are fully vectorizable bitwise, they can be implemented in parallel in single-cycle logic at the register level using 16-bit integer XOR. As a result, on a RISC general-purpose CPU any "presenting" iris code can be compared exhaustively against a large database of stored codes in search of a match at the rate of about 4 000 per second. (This clocked rate includes significant overhead due to complete iris code transfers, as well as table look-up to convert 16-bit integer XOR outcomes into running

sums of Hamming distance.) With dedicated hardware, fuller vectorization can be achieved and a further 40 000-fold speed-up in recognition is now possible. Since the decision process, including the calculation of confidence levels, relies only on computing the logical XOR vector between two iris codes comprising 2 048 bits, conventional SSI devices that have been available for decades at negligible cost offer the basis for immediate parallel implementation. For example, the simple 74F86 integrated circuit contains four independent XOR gates that can be clocked at 80 megahertz. Thus, a 32 x 32 array of 74F86 ICs (or a single equivalent dedicated gate array) could in principle execute comparisons and decisions at the rate of 160 million complete iris codes per second, if exhaustive database searches were required and if such databases existed.

Because of the speed of decision-making made possible by the commensurability of iris codes, it is not even necessary in this method for a Subject to make any claims about his identity (e.g., by entering a password, PIN, or swiping a card) that the biometric comparison then merely confirms or disconfirms. Rather, here he only needs to present his eye to the camera, and his identity is rapidly and automatically *determined* without any further interaction, by exhaustive search through a database that might be extremely large. As Shakespeare conveyed it much less mechanically in *The Merchant of Venice* (Act I, Scene 1), in the tradition of conceiving the eyes as windows to the soul, "Sometimes from her eyes I did receive fair speechless messages."

VI. CONCLUSION

Aristotelian philosophy held that the $\epsilon\iota\delta o\varsigma$ (ădos, distinguishing essence) of something resided in that quality which made it different from everything else. When we need to know with certainty who an individual is, or whether he is who he claims to be, we normally rely either upon something that he uniquely possesses (such as a key or a card), something that he uniquely knows (such as a password or PIN), or a unique biological characteristic (such as his appearance). Technologically the first two of these criteria have been the easiest to confirm automatically, but they are also the least reliable, since (in Aristotelian terms) they do not necessarily make this individual different from all others. Today, we hold that the uniqueness of a person arises from the trio of his genetic genotype, its expression as phenotype, and the sum of his experiences. For purposes of rapid and reliable personal identification, the first and third of these cannot readily be exploited: DNA testing is neither real-time nor unintrusive; and experiences are only as secure as testimony. The remaining unique identifiers are phenotypic characteristics. It is hard to imagine one better suited than a protected, immutable, internal organ of the eye, that is readily visible externally and that reveals random morphogenesis of high statistical complexity.

for providing the large photographic database of eye images on which this analysis was partially based.

REFERENCES

[1] F. H. Adler, *Physiology of the Eye: Clinical Application*, fourth ed. London: The C.V. Mosby Company, 1965.
[2] A. C. Bovik, M. Clark, and W. S. Geisler, "Multichannel texture analysis using localized spatial filters," *IEEE Trans. Pattern Anal. Machine Intell.*, vol. 12, pp. 55–73, 1990.
[3] R. Bright, *Smartcards: Principles, Practice, Applications.* New York: Ellis Horwood, Ltd., 1988.
[4] T. Caelli, "On discriminating visual textures and images," *Perception & Psychophysics*, vol. 31, pp. 149–159, 1982.
[5] ——, "Energy processing and coding factors in texture discrimination and image processing," *Perception & Psychophysics*, vol. 34, pp. 349–355, 1983.
[6] M. Clark and A. C. Bovik, "Experiments in segmenting text on patterns using localized spatial filters," *Pattern Recognit.*, vol. 22, pp. 707–717, 1989.
[7] J. M. Coggins and A. K. Jain, "A spatial filtering approach to texture analysis," *Pattern Recognit. Lett.*, vol. 3, pp. 195–203, 1985.
[8] J. G. Daugman, "Two-dimensional spectral analysis of cortical receptive field profiles," *Vision Res.* vol. 20, pp. 847–856, 1980.
[9] ——, "Uncertainty relation for resolution in space, spatial frequency, and orientation optimized by two-dimensional visual cortical filters," *J. Opt. Soc. Amer. A*, vol. 2, pp. 1160–1169, 1985.
[10] ——, "Complete discrete 2-D Gabor transforms by neural networks for image analysis and compression," *IEEE Trans. Acoust., Speech, Signal Processing*, vol. 36, pp. 1169–1179, 1988.
[11] H. Davson, *Davson's Physiology of the Eye*, 5th ed. London: Macmillan, 1990.
[12] L. Flom and A. Safir, U.S. Patent No. 4 641 349, U.S. Government Printing Office, Washington, DC, 1987.
[13] F. Galton, "Personal identification and description," *Nature* pp. 173–177, June 21, 1888.
[14] J. Ghosh, N. Gopal, and A. C. Bovik, "Textured image segmentation using localized receptive fields," in *Proc. Int. Joint Conf. Neural Networks*, vol. 2, 1990, pp. 283–286.
[15] R. M. Haralick, "Statistical and structural approaches to texture," *Proc. IEEE*, vol. 67, pp. 786–804, 1979.
[16] R. M. Haralick, K. Shanmugan, and I. Dinstein, "Textural features for image classification," *IEEE Trans. Syst., Man, Cybern.*, vol. 3, pp. 610–621, 1973.
[17] L. D. Harmon, M. K. Khan, R. Lasch, and P. F. Ramig, "Machine identification of human faces," *Pattern Recognit.*, vol. 13, pp. 97–110, 1981.
[18] A. K. Jain and F. Farrokhnia, "Unsupervised texture segmentation using Gabor filters," *Pattern Recognit.*, vol. 24, pp. 1167–1186, 1991.
[19] B. F. Logan, "Information in the zero-crossings of bandpass signals," *Bell Syst. Tech. J.*, vol. 56, pp. 487–510, 1977.
[20] S. G. Mallat, "A theory for multiresolution signal decomposition: The wavelet representation," *IEEE Trans. Pattern Anal. Machine Intell.*, vol. 11, pp. 674–693, 1989.
[21] Y. Meyer, "Principe d'incertitude, bases Hilbertiennes et algébres d'opérateurs," *Séminaire Bourbaki*, vol. 662, pp. 209–223, 1986.
[22] W. W. Peterson, T. G. Birdsall, and W. C. Fox, "The theory of signal detectability," *Trans. IRE* PGIT-4, pp. 171–212, 1954.
[23] M. Porat and Y. Y. Zeevi, "Localized texture processing in vision: Analysis and synthesis in the Gaborian space," *IEEE Trans. Biomed. Eng.*, vol. 36, pp. 115–129, 1989.
[24] J. Rohen, "Morphology and pathology of the trabecular meshwork," in *The Structure of the Eye*, Smelser, Ed. New York: Academic Press, 1961, pp. 335–341.
[25] A. Samal and P. A. Iyengar, "Automatic recognition and analysis of human faces and facial expressions: A survey," *Pattern Recognit.*, vol. 25, pp. 65–77, 1992.
[26] C. Shannon and W. Weaver, *Mathematical Theory of Communication.* Urbana, IL: Univ. of Illinois Press, 1949.
[27] W. P. Tanner and J. A. Swets, "A decision-making theory of visual detection," *Psychol. Rev.* vol. 61, pp. 401–409, 1954.
[28] A. Teuner and B. J. Hosticka, "Adaptive Gabor transformation for image processing," *IEEE Trans. Signal Processing*, in press, 1993.
[29] M. R. Turner, "Texture discrimination by Gabor functions," *Bio. Cybern.*, vol. 55, pp. 71–82, 1986.
[30] L. Van Gool, P. Dewaele, and A. Oosterlinck, "Texture analysis anno 1983," *Comput. Vision, Graphics, and Image Processing*, vol. 29, pp. 336–357, 1985.

[31] H. Wechsler, "Texture analysis—A survey," *Signal Processing*, vol. 2, pp. 271–282, 1982.
[32] N. Wiener, *Times Series.* Cambridge, MA: M.I.T. Press, 1949.
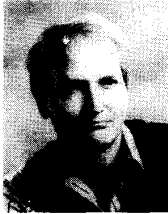
John G. Daugman received both the B.A. and Ph.D. degrees at Harvard University.

He subsequently joined the Faculty as Assistant Professor, teaching graduate and undergraduate courses in Electrical Engineering, Psychology, and Computer Science. His main research interests include multidimensional signal processing, computational neuroscience, pattern recognizing neural networks, and visual neurophysiology and perception.

Dr. Daugman is the author of about 40 publications in these fields, and he serves as Associate Editor of the journals IEEE TRANSACTIONS ON PATTERN ANALYSIS AND MACHINE INTELLIGENCE; IEEE TRANSACTIONS ON NEURAL NETWORKS; *Brain Research: Cognitive Brain Research*; and he is a member of the Executive Board of *Network: Computation in Neural Systems*. In 1988, he was awarded the Presidential Young Investigator Award by the U.S. National Science Foundation. In 1989, he became the inaugural holder of the Toshiba Endowed Chair in Computer Science at the Tokyo Institute of Technology, and in 1991, he was elected a Senior Research Fellow of the Faculty of Biology at Cambridge University, where he is a member of King's College and where he now directs research in computational neuroscience.